AGU PUBLICATIONS

Paleoceanography

RESEARCH ARTICLE
10.1002/2015PA002917

How well would modern-day oceanic property distributions be known with paleoceanographic-like observations?

Geoffrey Gebbie[1], Gregory J. Streletz[2], and Howard J. Spero[3]

[1]Department of Physical Oceanography, Woods Hole Oceanographic Institution, Woods Hole, Massachusetts, USA, [2]Institute for Data Analysis and Visualization, Department of Computer Science, University of California, Davis, California, USA, [3]Department of Earth and Planetary Sciences, University of California, Davis, California, USA

Key Points:
- Global property distributions can be reconstructed from data as sparse as that from the LGM
- Inference of past ocean properties is limited, however, with a sparse, proxy data set
- A state estimation method has skill at large spatial scales and outperforms optimal interpolation

Supporting Information:
- Data Set S1
- Supporting Information S1

Correspondence to:
G. Gebbie,
ggebbie@whoi.edu

Citation:
Gebbie, G., G. J. Streletz, and H. J. Spero (2016), How well would modern-day oceanic property distributions be known with paleoceanographic-like observations?, *Paleoceanography*, *31*, 472–490, doi:10.1002/2015PA002917.

Received 15 DEC 2015
Accepted 6 MAR 2016
Accepted article online 12 MAR 2016
Published online 8 APR 2016

Abstract Compilations of paleoceanographic observations for the deep sea now contain a few hundred points along the oceanic margins, mid-ocean ridges, and bathymetric highs, where seawater conditions are indirectly recorded in the chemistry of buried benthic foraminiferal shells. Here we design an idealized experiment to test our predictive ability to reconstruct modern-day seawater properties by considering paleoceanographic-like data. We attempt to reconstruct the known, modern-day global distributions by using a state estimation method that combines a kinematic tracer transport model with observations that have paleoceanographic characteristics. When a modern-like suite of observations (Θ, practical salinity, seawater $\delta^{18}O$, $\delta^{13}C_{DIC}$, PO_4, NO_3, and O_2) is used from the sparse paleolocations, the state estimate is consistent with the withheld data at all depths below 1500 m, suggesting that the observational sparsity can be overcome. Physical features, such as the interbasin gradients in deep $\delta^{13}C_{DIC}$ and the vertical structure of Atlantic $\delta^{13}C_{DIC}$, are accurately reconstructed. The state estimation method extracts useful information from the pointwise observations to infer distributions at the largest oceanic scales (at least 10,000 km horizontally and 1500 m vertically) and outperforms a standard optimal interpolation technique even though neither dynamical constraints nor constraints from surface boundary fluxes are used. When the sparse observations are more realistically restricted to the paleoceanographic proxy observations of $\delta^{13}C$, $\delta^{18}O$, and Cd/Ca, however, the large-scale property distributions are no longer recovered coherently. At least three more water mass tracers are likely needed at the core sites in order to accurately reconstruct the large-scale property distributions of the Last Glacial Maximum.

1. Introduction

Microfossils, such as planktonic (near-surface) or benthic (bottom-dwelling) foraminiferal shells from deep ocean sediments, contain a rich archive of chemical information that is related to changing ocean chemistry and circulation in Earth's past. Marine sediments record ocean circulation change at centennial to millennial timescales that are generally associated with large changes in regional and global climate [e.g., *Broecker and Denton*, 1989; *McManus et al.*, 2004; *Curry and Oppo*, 2005; *Piotrowski et al.*, 2008; *Gherardi et al.*, 2005, 2009; *McManus et al.*, 2004; *Waelbroeck et al.*, 2011; *Gherardi et al.*, 2009]. The spatial form and causes of past circulation changes, however, remain poorly understood due in part to observational difficulties [e.g., *Legrand and Wunsch*, 1995; *Liu et al.*, 2005; *Stouffer et al.*, 2006; *Huybers et al.*, 2007; *Keigwin and Boyle*, 2008; *Lisiecki et al.*, 2008]. A major issue is the sparsity of foraminiferal data, due to spatial limitations, such as their distribution along the fluid envelope (i.e., the sea surface, ocean margins, mid-ocean ridges, and bathymetric highs [*Divins*, 2003]), and the dissolution of calcium carbonate shells at abyssal locations below the lysocline [e.g., *Broecker and Peng*, 1982]. Also, the stratigraphic record of the buried fossils must be linked in the time domain despite the processes of winnowing, bioturbation, and slumping [e.g., *Keigwin and Guilderson*, 2009]. Retrieval of sediment cores is technically difficult, expensive, and time consuming, suggesting that paleoceanographic observations will remain sparse for the foreseeable future.

Perhaps more importantly, paleodata are typically derived from fossil geochemistry which covaries with oceanographic parameters of interest. These proxies are often an imperfect way to infer water properties from paleoceanographic environments. For example, an incomplete list of factors that influence the oxygen isotopic composition ($\delta^{18}O$) of calcium carbonate include the seawater temperature in which calcification occurred, the $\delta^{18}O$ of seawater [e.g., *Marchitto et al.*, 2014], seawater pH [e.g., *Spero et al.*, 1997], and vital

effects depending upon the species of foraminifera [e.g., *Bemis et al.*, 1998]. Further, the number of data types (usually from isotope or elemental ratios) that can be obtained in cores is smaller than the available observations of the modern-day ocean.

Analysis techniques honed on modern-day data, such as inverse methods, have been applied to the Last Glacial Maximum (i.e., LGM, 23 to 19 kyr before present) with mixed results. The paleodata have been shown to be consistent with a slowdown of the Atlantic meridional overturning circulation due to surface freshwater forcing [*Winguth et al.*, 2000], but these data were also shown to be consistent with the modern-day circulation [e.g., *Legrand and Wunsch*, 1995; *Gebbie and Huybers*, 2006; *Burke et al.*, 2011], calling into question the power of these particular paleodata to distinguish different scenarios. To constrain the overturning circulation rate, either data uncertainties need to be reduced by a factor of about 100 [*Huybers et al.*, 2007], a better initial guess of the LGM state is needed [*Kurahashi-Nakamura et al.*, 2014], or general circulation models must be improved [e.g., *Weber et al.*, 2007; *Brady et al.*, 2013]. A narrowed focus on water mass distributions and tracer distributions, however, permitted the glacial observations to rule out an unchanged modern-day circulation [*Gebbie*, 2014], giving promise that changes in glacial water mass geometry are quantifiable if the LGM is a near-equilibrium state.

Here we design a series of experiments to quantify how well glacial property distributions can be reconstructed given the special characteristics of paleodata. As the true glacial property distributions are not well known, we proceed by posing an idealized study where we determine how well modern-day ocean properties would be known if we were restricted to paleoceanographic-like observations. An experiment of this type previously found difficulties related to the lack of an accurate paleoceanographic rate constraint [e.g., *Huybers et al.*, 2007], so here our focus is on the steady state property distributions. While there is no formal distinction between state estimation methods and inverse box models, we refer to our reconstruction method as state estimation because mass and tracers follow the kinematic equations exactly, $\delta^{13}C_{DIC}$ (i.e., the $^{13}C/^{12}C$ ratio in dissolved inorganic carbon) is affected by organic carbon remineralization once waters leave the surface, and the chosen grid is similar to coarse-resolution general circulation models.

2. Experimental Design

The experimental design of this work is known in various fields as a cross validation [e.g., *Wahba and Wendelberger*, 1980], identical twin [e.g., *Köhl and Willebrand*, 2002], or observation system simulation [e.g., *McGillicuddy et al.*, 2001] experiment. A modern-day reference circulation and its associated suite of global tracer distributions is defined as the "truth" (section 2.1). We attempt to reconstruct the truth with a state estimation method (section 2.2) and a set of observations. In particular, "synthetic" or artificial observations are created by sampling the truth according to various paleodata characteristics (sections 2.3–2.5). The difference between the reconstructed and true fields is here interpreted as the "error." An additional experiment (section 2.6) is also described in order to test the primary (state estimation) reconstruction method against a simpler optimal interpolation method.

2.1. Reference or True Solution

We define the true solution to be a modern-day reference state estimate for a suite of seven tracers: temperature, salinity, phosphate, dissolved oxygen, nitrate, the stable carbon isotope ratio ($^{13}C/^{12}C$ or $\delta^{13}C_{DIC}$), and seawater oxygen isotope ratio ($^{18}O/^{16}O$ or $\delta^{18}O_w$) [*Gebbie*, 2014]. This state estimate includes the first three-dimensional gridded distribution of $\delta^{13}C_{DIC}$ with global coverage that is constrained by seawater data (Global Data Analysis Project and Carbon in the Atlantic project) [*Key et al.*, 2004, 2010] as compiled by *Schmittner et al.* [2013]. The reference deep $\delta^{13}C_{DIC}$ spatial distribution is strongly anticorrelated with the phosphate concentration (Figure 1), where the remineralization of organic particles links a source of phosphate with a sink of $\delta^{13}C_{DIC}$ through the Redfield ratio and carbon isotope fractionation during photosynthesis [e.g., *Broecker and Maier-Reimer*, 1992]. Therefore, $\delta^{13}C_{DIC}$ values decrease as organic matter is remineralized, and the $\delta^{13}C$ spatial pattern is indicative of accumulation of organic carbon and water mass aging (i.e., increase in elapsed time since water was at the surface) from the North Atlantic to the North Pacific. Air-sea gas exchange at the ocean surface also affects $\delta^{13}C_{DIC}$, and thus, the major southern and northern water masses, Antarctic Bottom Water and North Atlantic Deep Water (NADW), have distinct values. In the Atlantic, $\delta^{13}C_{DIC}$ clearly delineates the incursion of NADW into the South Atlantic (Figure 2). Later in this work, our diagnostics will focus on deep ocean and Atlantic distributions because they can be interpreted in terms of physical processes like aging and water mass formation.

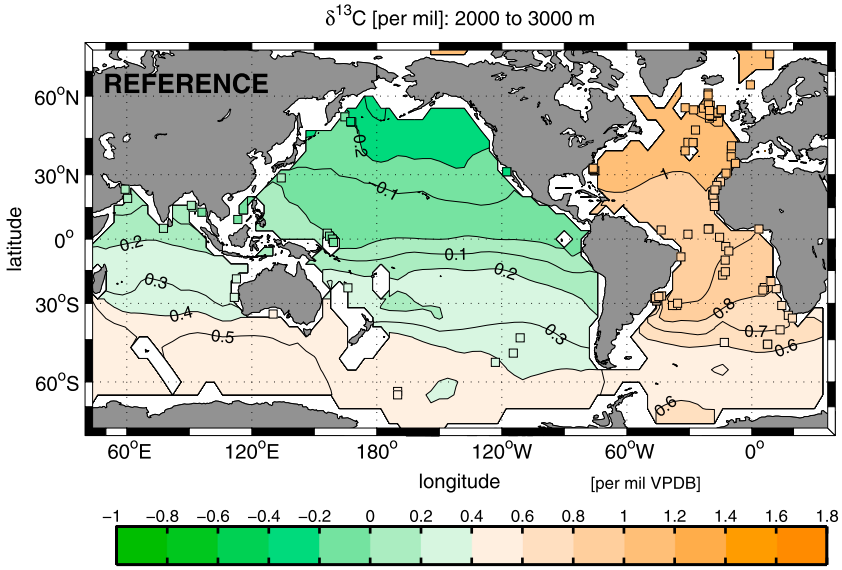

Figure 1. Distribution of $\delta^{13}C_{DIC}$ averaged between 2000 and 3000 m depth in the modern-day reference solution (truth). Observations in this depth range (squares) are colored according to the $\delta^{13}C_{DIC}$ value at each point. (The full observational data set is discussed later.)

The other tracers in the reference suite are consistent with the same circulation field as $\delta^{13}C_{DIC}$. The temperature, salinity, phosphate, dissolved oxygen, and nitrate distributions fit the World Ocean Circulation Experiment global hydrographic atlas within its reported uncertainties [*Gouretski and Koltermann*, 2004]. $\delta^{18}O_w$ is fit within 0.12‰ of the pointwise modern-day samples below 1 km depth, near the observational error given by *Schmidt* [1999]. The grid has 4° × 4° horizontal resolution and 33 vertical levels. Note that the colored squares in Figure 2 are located at the latitude and depth of the Atlantic observations, but their colors do not perfectly match the background color because of the zonal variability not captured by the basinwide zonal average background fields. The standard deviation of zonal variability is roughly 0.2–0.3‰ in the thermocline and 0.05‰ or less in the deep ocean and thus rivals the observational uncertainty.

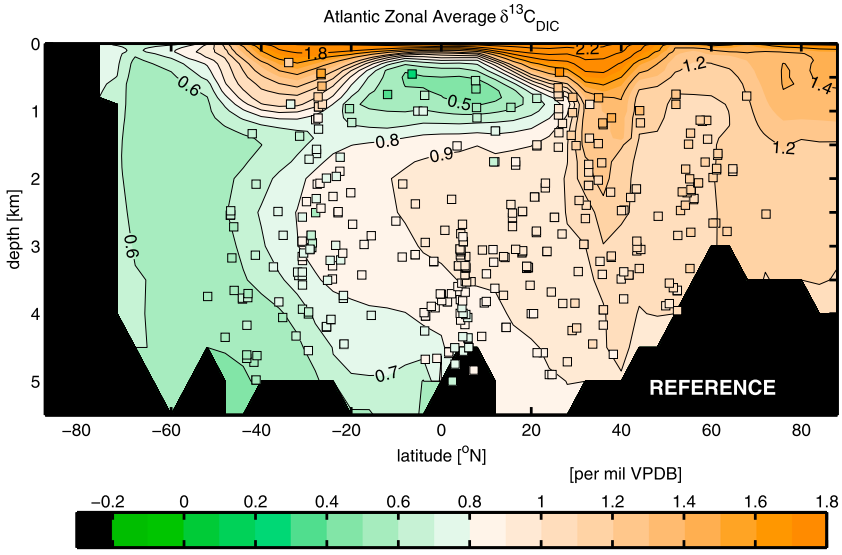

Figure 2. Zonally averaged basinwide Atlantic section of reference $\delta^{13}C_{DIC}$. All Atlantic observations (squares) are colored according to the $\delta^{13}C_{DIC}$ value at each point. Note that the color scale is slightly adjusted relative to Figure 1. The deepest Atlantic bathmetry at each latitude is plotted.

Table 1. List of the Control Variables in the State Estimation Method: (Column 1) Symbol, (Column 2) Full Written Name, (Column 3) Any Restrictions for the Variable Being Adjusted, and (Column 4) the A Priori Uncertainty Given the First Guess of These Controls Including a Smoothness Constraint of the Form Used by *Gebbie et al.* [2006][a]

Control Variable (Units)	Long Name	Description	Uncertainty
Θ (°C)	Conservative Temperature	Surface boundary conditions	11.2°C
S_* (g/kg)	Preformed salinity	Surface boundary conditions	2.2 g/kg
$\delta^{18}O_w$ (‰ VSMOW)	$^{18}O/^{16}O$ ratio of H_2O	Surface boundary conditions	1.2‰ VSMOW
PO_4^{3-} (μmol/kg)	Phosphate	Surface boundary conditions	0.6 μmol/kg
NO_3^- (μmol/kg)	Nitrate	Surface boundary conditions	10.7 μmol/kg
O_2 (μmol/kg)	Dissolved oxygen	Surface boundary conditions	56.8 μmol/kg
$\delta^{13}C_{DIC}$ (‰ VPDB)	$^{13}C/^{12}C$ ratio of DIC	Surface boundary conditions	0.5‰ VPDB
m ( )	Mass flux ratios	Subset that conserves mass	$\pm^{150\times}_{1/150\times}$
q (μmol/kg)	Remineralized PO_4	All interior locations	$\pm^{50\times}_{1/50\times}$

[a]The uncertainties are chosen by the standard deviation of the misfit between the first-guess and true fields and are much larger than the observational uncertainties. The control vector uncertainty is large so that little prior information is used to form the reconstructions. For the mass flux ratios and remineralization sources, the uncertainty is applied in a lognormal sense. The error bars for mass flux ratios (remineralization sources) span from $150 \times m$ ($50 \times q$) to $1/150 \times m$ ($1/50 \times q$). VSMOW is Vienna Standard Mean Ocean Water, and VPDB is Vienna Pee Dee Belemnite.

2.2. Reconstruction Method

Before detailing the observations that are taken, we start by introducing the reconstruction method that can be applied to any combination of observations. Here we seek three-dimensional property distributions that fit the observations within uncertainty and also satisfy steady state tracer equations, such as the conservation of mass and tracer, using the method described by *Gebbie* [2014] and in Appendix B. The steady state constraints provide a simple framework for making global reconstructions, although the steady state assumption has been shown to be the largest source of errors when estimating modern-day transports [*Ganachaud*, 2003]. Here we sidestep the issue of estimating transports by dividing each tracer equation by the total mass flux into the grid cell [i.e., *Gebbie and Huybers*, 2012], thus reducing the constraints into the form of a static water mass mixing model for each seawater property:

$$c_j = \sum_{i=1}^{N} m_{ij} c_i + q_j, \tag{1}$$

where c_j is the tracer concentration in grid cell j; there are N neighboring grid cells with concentration, c_i; m_{ij} is the ratio of mass flux from i to j relative to all fluxes into j and is bounded between zero and one; and q_j is a nonconservative source in j (see Appendix A for more details). Rather than solving for advective and diffusive fluxes explicitly, we obtain the mass flux ratios, m_{ij}, that are interpretable as the fraction of water coming from each neighbor by the combined effect of advection and diffusion. The problem is solved using a constrained least squares method that first determines the optimal water mass geometry, surface boundary conditions for all tracers, and the remineralization at each subsurface grid cell (the "controls" of the problem, Table 1). Given the controls, the kinematic tracer model can reconstruct 3-D global property distributions for all of the state variables (listed in Table 2).

The tracers are divided into those that are treated as perfectly conservative (Conservative Temperature [Θ], preformed salinity [S_*], and $\delta^{18}O_w$) and those subject to nonconservative effects due to remineralization ($\delta^{13}C_{DIC}$, PO_4, NO_3, and O_2). Nonconservative terms are related by a prescribed stoichiometric ratio. Note that the isotope ratios are modeled as if they are one physical quantity and not a ratio of two quantities, which normally incurs an error. Here the true distributions were produced by using the same model and thus are statistically consistent with the reconstruction method. For the results of this perfect model scenario to be applicable to real-world examples, however, potential model error would have to be addressed.

If observations lack information about a certain region, the reconstruction will revert to the prior assumptions. The first-guess fields were chosen as if approaching the Earth as an unexplored planetary object. The first-guess temperature is applied at the sea surface and assumes that the insolation is Earth-like, and thus,

Table 2. List of the State Variables of the Model by (Column 1) Symbol, (Column 2) Full Written Name, (Column 3) the First Guess for the State Vector Surface Boundary Condition, and (Column 4) Nonconservative Effects Due To Interior Sources or Sinks of Remineralized Material[a]

State Variable (Units)	Long Name	First Guess	Interior Sources
Θ (°C)	Conservative Temperature	sea surface temperature = 30°C × cos(λ)	none
S_* (g/kg)	preformed salinity	modern-day global surface mean	none
$\delta^{18}O_w$ (‰ VSMOW)	$^{18}O/^{16}O$ ratio of H_2O	modern-day global surface mean	none
PO_4^{3-} (μmol/kg)	phosphate	modern-day global surface mean	q
NO_3^- (μmol/kg)	nitrate	modern-day global surface mean	15.5 q
O_2 (μmol/kg)	dissolved oxygen	$O_2 = O_2^{SAT}(T)$	−170 q
$\delta^{13}C_{DIC}$ (‰ VPDB)	$^{13}C/^{12}C$ ratio of DIC	$\delta^{13}C_{DIC} = 2.7 - 1.1\ PO_4$	−1.1 q
m ( )	mass flux ratios	uniform for each grid cell	-
q (μmol/kg)	remineralized PO_4	3×10^{-4} μmol/kg	-

[a]Conservative Temperature, Θ, is guessed to vary with latitude: 30°C × cos(λ), where λ is latitude in degrees. The first-guess fields for S_*, $\delta^{18}O_w$, PO_4, NO_3, and O_2 are set to be uniformly equal to modern-day global surface mean. $\delta^{13}C_{DIC}$ set such that the air-sea component [e.g., *Lynch-Stieglitz et al.*, 1995] is equal to zero. The first-guess oxygen field is equal to the saturation value at the first-guess temperature. The mass flux ratios are equal to $1/N$, where N equals the number of neighboring cells, approximating a purely diffusive circulation. The remineralization rate is set to an arbitrary small value for numerical reasons, as this rate is nonnegative and handled as a logarithm that cannot be strictly zero.

the temperature varies with latitude over a range of 0°C to 30°C. The first guess for oxygen assumes saturation with respect to the first-guess temperature. The first-guess fields for S_*, $\delta^{18}O_w$, PO_4, NO_3, and O_2 are set to be uniformly equal to modern-day global surface mean at the model surface. The first-guess $\delta^{13}C_{DIC}$ is set assuming that the air-sea component [e.g., *Lynch-Stieglitz et al.*, 1995] is zero at the surface. Mass flux ratios that describe the movement of seawater are chosen to be uniform in each grid cell, thus approximating a purely diffusive circulation (see Appendix A1). Note that little prior information is used here and that a realistic LGM case may actually be easier to formulate because modern-day information is available to form a first guess.

2.3. SPARSE Experiment

The first experiment, labeled "SPARSE," is designed to isolate the impact of sparsity on a global reconstruction. Imperfect "observations" are made from the true solution at 492 core sites contained in the *Peterson et al.* [2014] compilation along with additional cores and quality controlling by *Gebbie et al.* [2015]. We make an observation of the modern-day seafloor water properties at the locations where a benthic $\delta^{13}C$ and $\delta^{18}O$ value dated to the LGM (23 to 19 kyr before present) exists in the latest compilation (Figure 3). The SPARSE experiment samples the full suite of modern-day tracers so that only the sparsity of observations is being tested (see Table 3). The observational step is modeled by projecting the true distribution onto the observational locations using a linear interpolation or extrapolation from the eight nearest grid points. Then, noise is independently added to each observation according to a Gaussian distribution with standard deviation given by the true data uncertainty (see "Uncertainty" in Table 3).

The mean distance from a grid point to the nearest observation is 1250 km horizontally and 71 m in vertical (Figure 4). (The median distance is 1134 km and 5 m, respectively.) The most energetic ocean circulation lengthscales, on the other hand, are in the mesoscale (200 km horizontally) as diagnosed from the wavenumber spectrum of a satellite altimeter [e.g., *Stammer*, 1997]. In the time mean, much of mesoscale variability should vanish except near boundaries and topographic features. The typical distance to an observation exceeds the intrinsic lengthscale of the fluid, strictly speaking, and thus, the paleodata qualifies as sparse by this metric.

The reconstruction method of section 2.2 is implemented with the imperfect observations. Five different reconstructions are produced with different noise realizations. The five trials are averaged and used in the diagnostics that follow. Five trials are not enough to capture the degrees of freedom in the 492 observational locations, but the computational expense of finding a converged solution is high. For example, each SPARSE experiment requires nearly 10,000 model executions to find an acceptable solution, as the problem is highly nonlinear due to the uncertain mass flux ratios multiplying the uncertain tracer fields in equation (1).

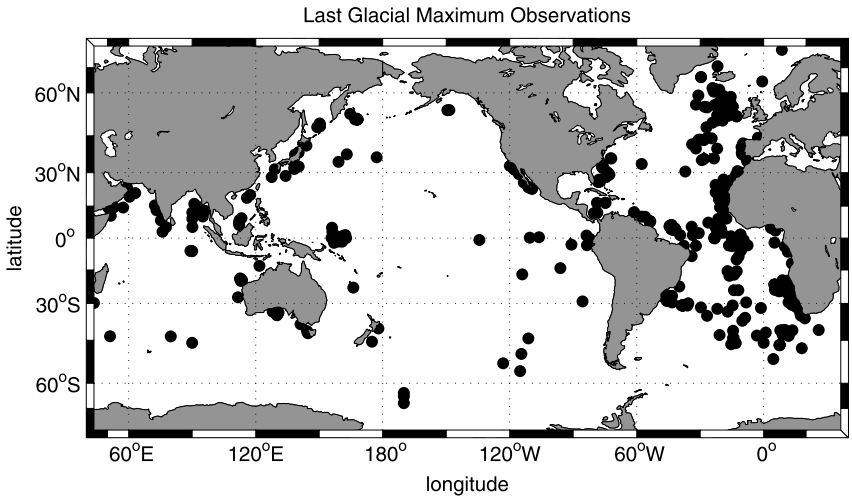

Figure 3. The 492 seafloor sites with paleoceanographic data (δ^{13}C and δ^{18}O values as recorded by benthic foraminifera) as compiled by *Peterson et al.* [2014] and *Gebbie et al.* [2015]. Note the irregular sampling as demanded by the availability of sediment. Also note the vast swaths of the world ocean, including much of the Pacific, Indian, and Southern Oceans, that are not sampled.

2.4. PROXY Experiment

The LGM data are also limited in that they indirectly measure seawater properties through a proxy relationship. Hence, we define the "PROXY" experiment to answer the question of how well the modern-day circulation is recovered when only paleoproxies (δ^{13}C of calcite [$\delta^{13}C_c$], δ^{18}O of calcite [$\delta^{18}O_c$], and seawater Cd concentration [Cd_w]) are observed (see Table 4). To isolate the effect of the proxy observations and to remove the effect of sparsity, we observe the three proxy tracers at all grid cells. Benthic foraminiferal $\delta^{13}C_c$ observations are constructed by assuming that they reflect $\delta^{13}C_{DIC}$ with noise that has a standard deviation of 0.15‰ and zero mean, consistent with assumptions used by previous investigators [e.g., *Duplessy et al.*, 1984; *Marchal and Curry*, 2008]. This assumed error is an optimistic value that encapsulates both measurement and representation error. Synthetic observations of $\delta^{18}O_c$ are produced from $\delta^{18}O_w$ and temperature with the relation, $\delta^{18}O_c = \delta^{18}O_w - 0.224 \times T + 3.53 + n$ [*Marchitto et al.*, 2014], thus representing the calcification of foraminiferal calcite shells where n represents noise (again taken to be Gaussian with standard deviation of 0.15‰). Cadmium observations are synthetically taken following a particle-formation chemical fractionation model: $Cd_w = 1.2/\{2[(3.3/PO_4)\ -1]+1\} + n$ [*Elderfield and Rickaby*, 2000], where the standard deviation of the noise is 0.08 nmol/kg. Here we focus on the fact that the proxies indirectly measure physical quantities and choose to ignore any possible systematic or structural error in these equations themselves. Coretop calibration studies [e.g., *Marchal and Curry*, 2008], culturing studies [*Spero et al.*, 1997], and plankton tow studies on planktonic foraminifera [*Peeters et al.*, 2002] suggest that the error in doing so may be considerable. Again, the state estimation method is run five times to account for five different realizations of noisy observations.

Table 3. Observations for the SPARSE Experiment, Listed by the Symbolic Name (Column 1), Written Name (Column 2), the Source of the Global, Three-Dimensional Distribution Designated as the Truth (Column 3), the Original Source of the Observations to Create the True Gridded Distributions (Column 4), and the Uncertainty for Each Observation (Column 5)

Data Type	Long Name	Truth	Original Source	Uncertainty
θ	potential temperature	*Gebbie* [2014]	*Gouretski and Koltermann* [2004]	0.44°C
S_P	practical salinity	*Gebbie* [2014]	*Gouretski and Koltermann* [2004]	0.17 [PSS-78]
PO_4^{3-}	phosphate	*Gebbie* [2014]	*Gouretski and Koltermann* [2004]	0.13 µmol/kg
NO_3^-	nitrate	*Gebbie* [2014]	*Gouretski and Koltermann* [2004]	1.6 µmol/kg
O_2	dissolved oxygen	*Gebbie* [2014]	*Gouretski and Koltermann* [2004]	11.3 µmol/kg
$\delta^{18}O_w$	$^{18}O/^{16}O$ ratio of H_2O	*Gebbie* [2014]	*Schmidt et al.* [1999]	0.2‰ VSMOW
$\delta^{13}C_{DIC}$	$^{13}C/^{12}C$ ratio of DIC	*Gebbie* [2014]	*Schmittner et al.* [2013]	0.15‰ VPDB

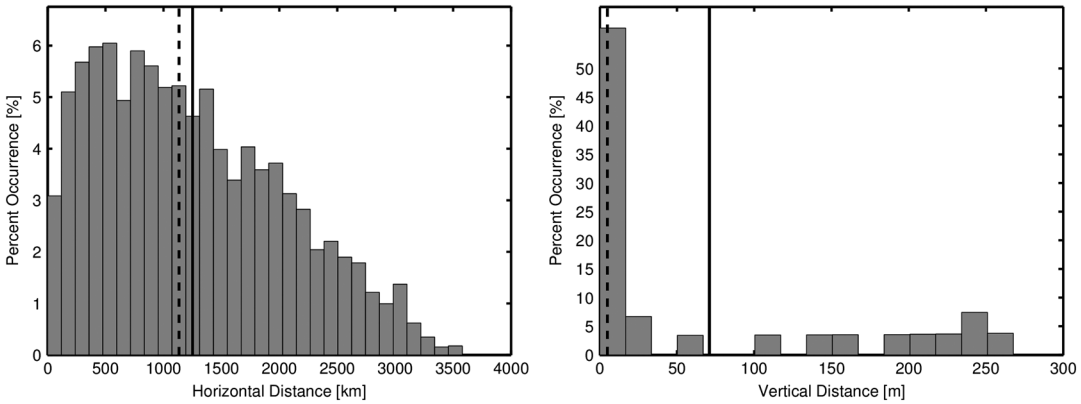

Figure 4. (left) Horizontal and (right) vertical distances from each grid point to the nearest observation. The mean (solid black line) and median (dashed line) distances are also included.

2.5. SPARSE+PROXY Experiment

The most realistic analog to the LGM case is here defined as the "SPARSE+PROXY" experiment. How well is the modern-day circulation recovered when only the paleoproxies, $\delta^{13}C_c$, $\delta^{18}O_c$, and Cd_w, are observed at the paleodata locations? This experiment is already optimistic, as Cd_w is only available at a subset of the 492 locations (75 reported by *Marchitto and Broecker* [2006] and 87 used by *Gebbie* [2014]). The state estimation procedure is run five times, and the resulting property distributions are again averaged. This experiment aims to account for both the sparse and proxy nature of paleoceanographic observations.

2.6. Optimal Interpolation Experiment

The technique of optimal interpolation (more accurately known as "objective mapping" because it is actually an approximation method [e.g., *Bretherton et al.*, 1976; *Troupin et al.*, 2012]) is standard for producing maps in physical oceanography and paleoceanography [e.g., *Curry and Oppo*, 2005] and is related to kriging and ridge regression used in other geosciences. The Optimal Interpolation (OI) experiment is formulated as a baseline to evaluate the skill of the state estimation method. Optimal interpolation is implemented by treating each property distribution as being independent, and thus, we focus on the $\delta^{13}C_{DIC}$ tracer alone. Here we feed the OI algorithm, the $\delta^{13}C$ observations from the SPARSE experiment, and the correct noise statistics on those observations (see Appendix C). The statistics of the covariance of the $\delta^{13}C_{DIC}$ field are also given to the algorithm in the effort to make the resulting field as smooth as possible without degrading the fit to the observations. To this end, the supplied vertical lengthscale varies from 100 m at the surface to 3000 m at the seafloor and is chosen to represent the increased stratification and decreased vertical covariance in the upper ocean. The horizontal lengthscale is 28° of longitude or latitude, which is approximately 3000 km meridionally and varies in the zonal direction from 3000 km at the equator to 100 km at the poles. In a realistic scenario, these characteristics may not be accurately known, and the skill of an actual OI implementation would be lower. On the other hand, a cross-validation approach can improve the skill of OI with only the observational information (G. J. Streletz et al., Interpolating sparse scattered data using flow information, submitted to *Journal of Computational Science*, 2016), but we have not used such a sophisticated method here. While OI permits a closed form solution for the expected solution and its uncertainty, here we prefer to keep the analysis consistent with the state estimation experiments by performing and averaging five trials.

Table 4. Observations for the PROXY and SPARSE+PROXY Experiments, Listed by the Symbolic Name (Column 1), Written Name (Column 2), the Source of the Global, Three-Dimensional Distribution Designated as the Truth (Column 3), the Reference for the Proxy Equation Used to Create the Synthetic Observations and the Reconstructions (Column 4), and the Observational Uncertainty (Column 5)[a]

Data Type	Long Name	Truth	Proxy Equation	Uncertainty
$\delta^{18}O_c$	$^{18}O/^{16}O$ ratio of calcite	*Gebbie* [2014]	*Marchitto et al.* [2014]	0.15‰ VSMOW
$\delta^{13}C_c$	$^{13}C/^{12}C$ ratio of calcite	*Gebbie* [2014]	*Duplessy et al.* [1984]	0.15‰ VPDB
Cd_w	inferred seawater Cd concentration	*Gebbie* [2014]	*Elderfield and Rickaby* [2000]	0.08 nmol/kg

[a]The observational uncertainty is used in two consistent ways: (1) to add noise to the synthetic observations and (2) to provide statistics to the reconstruction method through the **W** matrix of equation (B1).

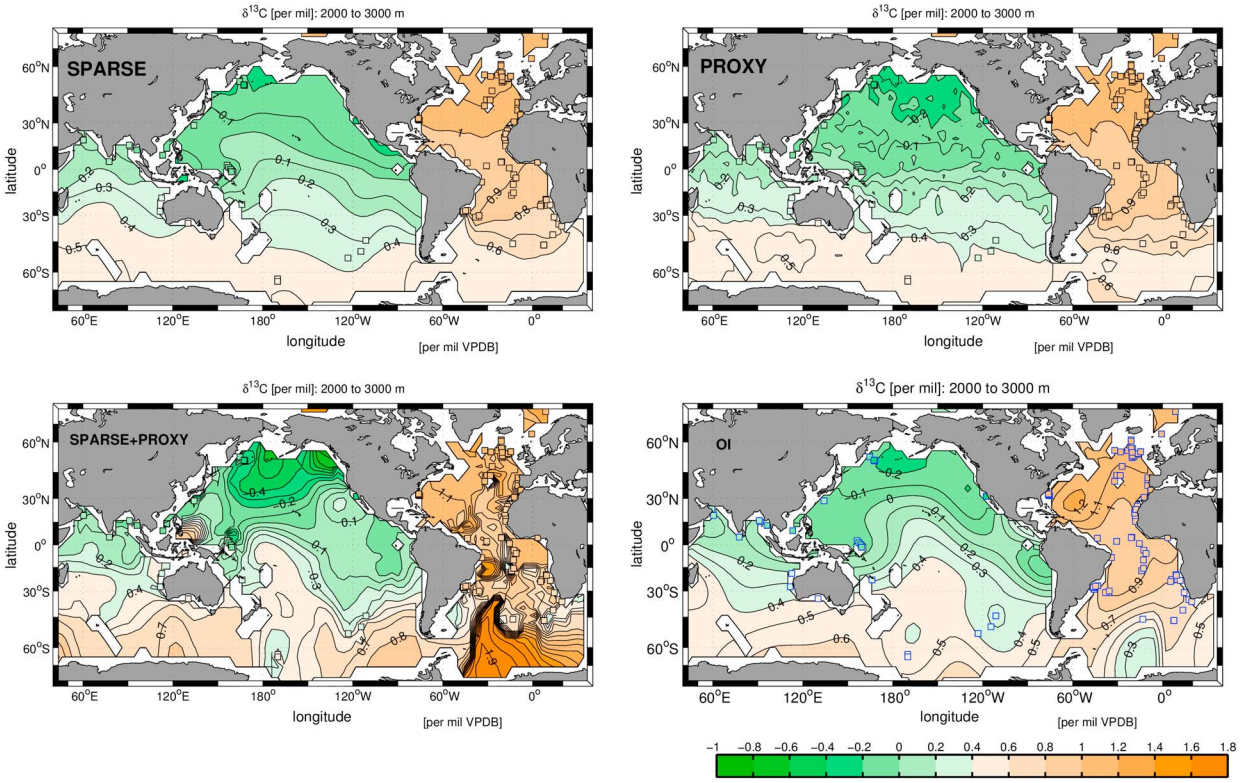

Figure 5. Deep ocean $\delta^{13}C_{DIC}$ distribution averaged between 2 and 3 km depth (background contours) for the following cases: (top left) SPARSE, (top right) PROXY, (bottom left) SPARSE+PROXY, and (bottom right) OI. Observations in this depth range (colored squares) are on the same color scheme as the background field. Compare to the true distribution in Figure 1.

3. Results

3.1. Deep Ocean

All reconstructions (SPARSE, PROXY, SPARSE+PROXY, and OI) capture the basic deep ocean contrast between high Atlantic and low Pacific $\delta^{13}C_{DIC}$ values (Figure 5). Thus, the global scale is reconstructed from 492 observations regardless of sophistication of method. At smaller scales, differences emerge between the reconstructions. While both the SPARSE and PROXY results appear to match the true spatial structure well, the SPARSE result is smoother in part because the use of additional tracers permits noise to be filtered out of the observations. On the other hand, the PROXY experiment admits more noise in the trade-off of fitting the data more closely. Both the SPARSE+PROXY and OI experiments permit much more regional spatial structure in data-poor regions, indicating that results of extrapolation are not well constrained. Problems are severe enough in the SPARSE+PROXY experiment that the overall range of $\delta^{13}C_{DIC}$ is overestimated, with values approaching 2.0‰ in the Southern Ocean and as low as −0.4‰ in the North Pacific. The experiments demonstrate that the sparsity and proxy nature of paleo-observations are not a problem individually, but observations with both characteristics have limited ability to constrain large-scale distributions.

The apparent aging of deep ocean waters from Atlantic to the Pacific is seen in the reference $\delta^{13}C_{DIC}$ and is reconstructed in the SPARSE and PROXY cases. Determining the spreading of $\delta^{13}C_{DIC}$ (and net direction of tracer transport) in the Southern Ocean is challenging due to the small horizontal gradients in the zonal direction, but SPARSE and PROXY cases correctly indicate the maximum Southern Ocean $\delta^{13}C_{DIC}$ in the Atlantic sector and a gradual decrease into the Indian and Pacific sectors, suggesting that the Atlantic and Pacific are linked along a eastward path in the Southern Ocean. Large Southern Ocean lateral inhomogeneities are present in SPARSE+PROXY and OI experiments, and the magnitude of these spurious signals overwhelms the presence of any water mass spreading. The OI case is unencumbered by constraints such as mass conservation or the geographic coherence of tracer plumes, which can partially explain the result. The similarity in the results of the kinematically consistent SPARSE+PROXY experiment, however, suggests that the lack of Southern Ocean observations is the bigger limitation. Thus, the inference of circulation pathways from $\delta^{13}C_{DIC}$

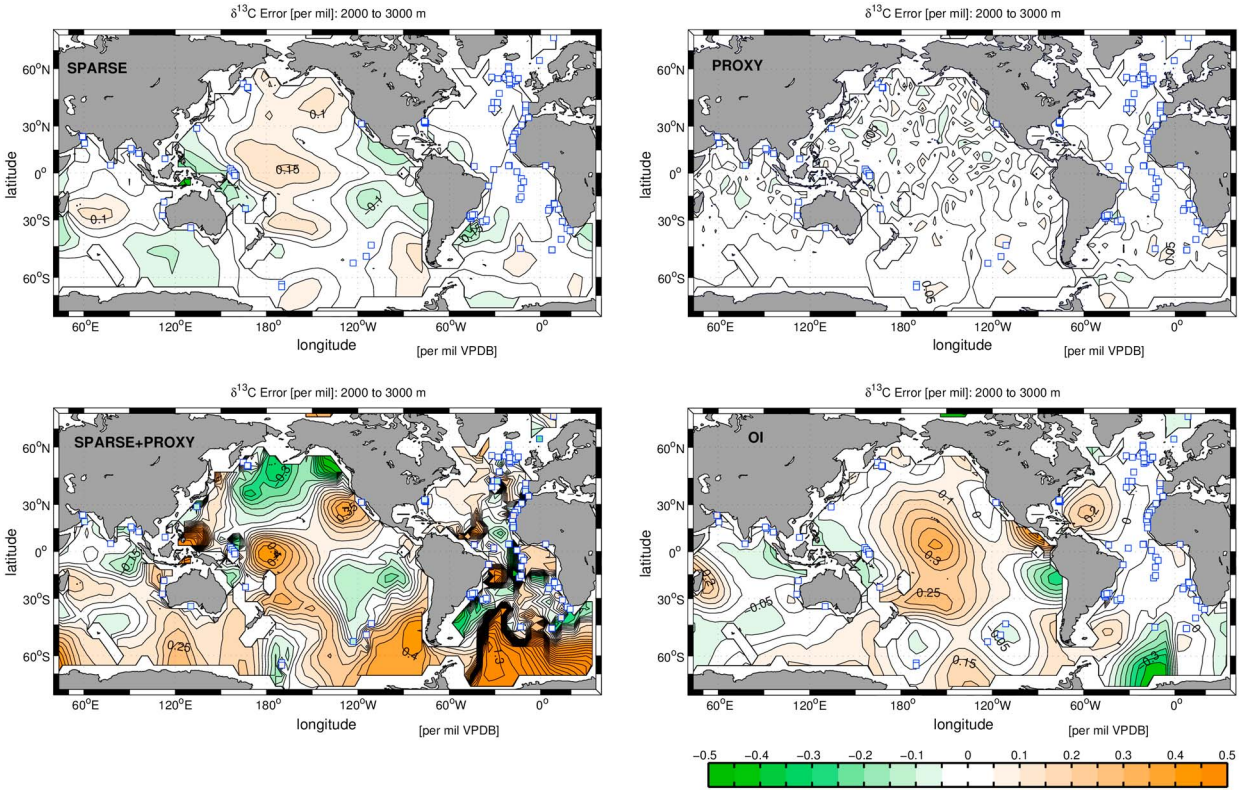

Figure 6. Deep ocean $\delta^{13}C_{DIC}$ errors averaged between 2 and 3 km depth and defined as the difference between the reconstructed distributions and the truth: (top left): SPARSE, (top right) PROXY, (bottom left) SPARSE+PROXY, and (bottom right) OI cases. The pointwise misfit or error is reproduced for observational locations in this depth range (colored squares). Compare to the true distribution in Figure 2.

alone is difficult, both due to physical reasons such as the incorporation of southern source waters with distinct signals [*Gebbie et al.*, 2015] and due to the lack of observational constraints.

The difference between the reconstructed and withheld true distribution is diagnosed as the $\delta^{13}C_{DIC}$ error (Figure 6). The PROXY experiment has errors that are almost always less than 0.05‰, showing reduced errors relative to the $\delta^{13}C_{DIC}$ uncertainty of 0.15‰ in each trial. For all experiments, errors are small near the observations, as expected. In the western Pacific, a large open-ocean region is unconstrained by data and is a good case study for the extrapolation skill of the experiments. Aside from the PROXY case, the SPARSE case has the smallest errors that are no larger than 0.15‰, while the SPARSE+PROXY and OI cases have errors of 0.4‰ in the western Pacific that are systematically too high and can be explained by the applied prior assumptions. The state estimation method starts from a first guess with mass flux ratios that are nearly uniform, as would arise from an ocean with modern-like eddy diffusivities but vanishingly small velocities (see Appendix A1 for details). This first guess permits communication of high-$\delta^{13}C_{DIC}$ surface values to the deep through diffusive processes. For the other case, the OI method reverts to the global mean $\delta^{13}C_{DIC}$ value of 0.8‰ which corresponds to a positive anomaly in this region. Errors are even larger elsewhere, such as the conspicuous large error in Atlantic sector of the SPARSE+PROXY experiment that will be addressed in the next section.

3.2. Atlantic Section

The Atlantic Ocean $\delta^{13}C_{DIC}$ distribution, depicted as a basinwide average including the Mediterranean and Caribbean Seas (Figure 7), does not simply reflect aging of the circulation but instead indicates water mass mixing. The sandwiching of enriched-$\delta^{13}C_{DIC}$ northern source waters between depleted-$\delta^{13}C_{DIC}$ southern source waters is reconstructed in the SPARSE, PROXY, and OI experiments. In the failed SPARSE+PROXY case, the state estimation method finds an alternate scenario that also fits the data. This solution is symmetric about the equator, where the basic gradient is not between northern and southern source waters, but instead between new surface waters and old deep waters. For this reason, the relatively young Southern Ocean waters have $\delta^{13}C_{DIC}$ values that are much too high, explaining the large errors previously seen in the Atlantic

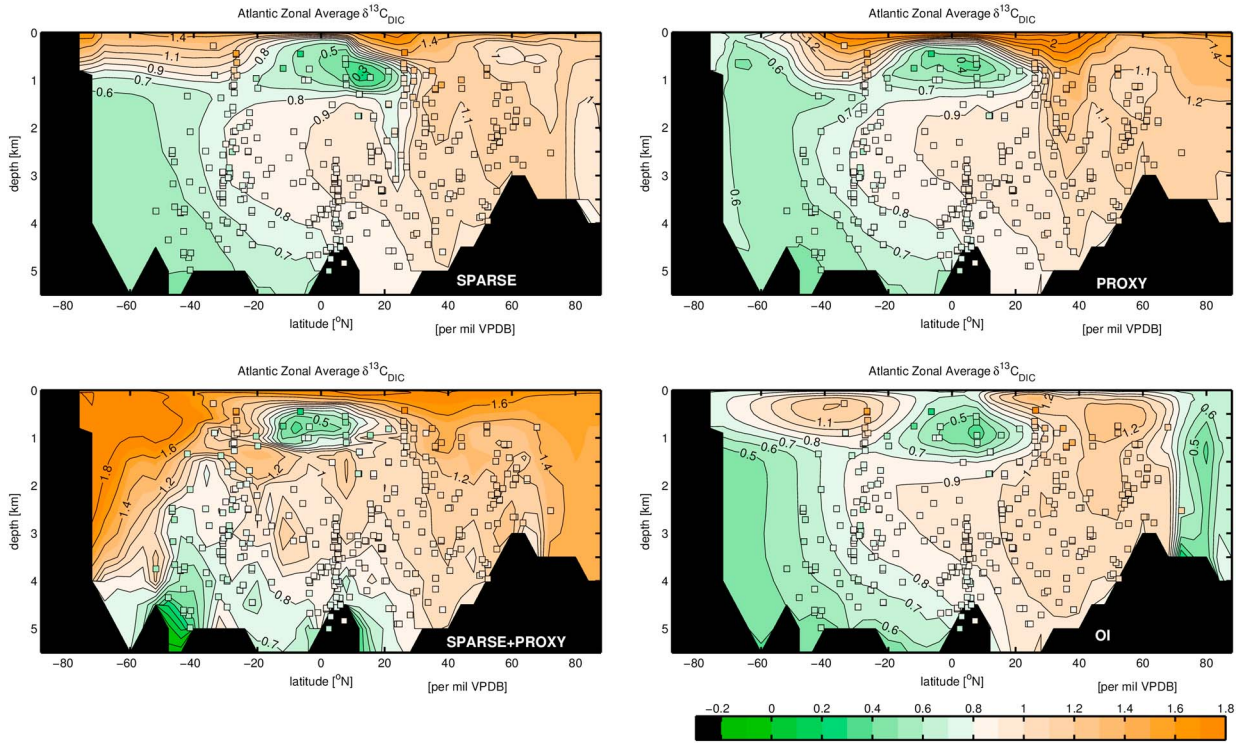

Figure 7. Basinwide zonal average Atlantic $\delta^{13}C_{DIC}$ (contours and background colors) for the following cases: (top left) SPARSE, (top right) PROXY, (bottom left) SPARSE+PROXY, and (bottom right) OI. Observations in this longitudinal range (colored squares) are all taken along the seafloor even though they appear to be midwater column. The deepest bathymetry in the entire zonal swath is plotted. The contour interval increases from 0.1‰ to 0.2‰ above 1.8‰ for visibility at the surface.

sector. Such a failure should not be considered due to a faulty methodology but rather reflects the ambiguity inherent in sparse, proxy observations.

The tropical $\delta^{13}C_{DIC}$ minimum at 1000 m depth due to the incursion of Antarctic Intermediate Water and accumulation of remineralized carbon in the pycnocline is also captured, suggesting that most of the reconstructions can disentangle water mass and remineralization signals. In experiments without the four intermediate depth cores at the Demerara Rise (500–1000 m depth, 4°N), the volume of waters with $\delta^{13}C_{DIC}$ depleted below 0.8‰ was roughly halved (not shown), indicating that these cores sample a key region for ocean basin reconstructions.

The OI case fits the observations quite closely and is able to successfully reconstruct many of the Atlantic features due to the good data coverage. There are closed contours of high-$\delta^{13}C$ waters (> 1.1‰) near the subtropical ocean surface, however, and such closed contours violate the steady state advection-diffusion equation with any value of positive diffusivity [e.g., *Gebbie and Huybers*, 2010]. The tongue of Antarctic Intermediate Water that connects the Southern Ocean surface and the tropical $\delta^{13}C_{DIC}$ minimum is also difficult to see because of the smoothness of the reconstruction away from data. Thus, the standard OI reconstruction method does quite well at reconstructing property distributions but has limitations for interpreting the underlying circulation.

The Atlantic section $\delta^{13}C_{DIC}$ errors tell a story consistent with the previous deep ocean analysis that the SPARSE and PROXY experiments are successful at reconstructing the global property field everywhere below 1 km depth but that the SPARSE+PROXY experiment is not (Figure 8). For all cases, the $\delta^{13}C_{DIC}$ values at the actual observational sites are nearly perfect, as indicated by the white squares in the figure. Again, the PROXY experiment has errors below 0.05‰. The SPARSE experiment errors grow as large as 0.5‰ in the upper kilometer. Both the SPARSE+PROXY and OI cases have this surface-intensified error and also have errors in the polar regions due to inaccurate extrapolation. As described above, the SPARSE+PROXY error in the Southern Ocean is greater than 1‰ and is explained by a complete reorganization of circulation. There is no obvious

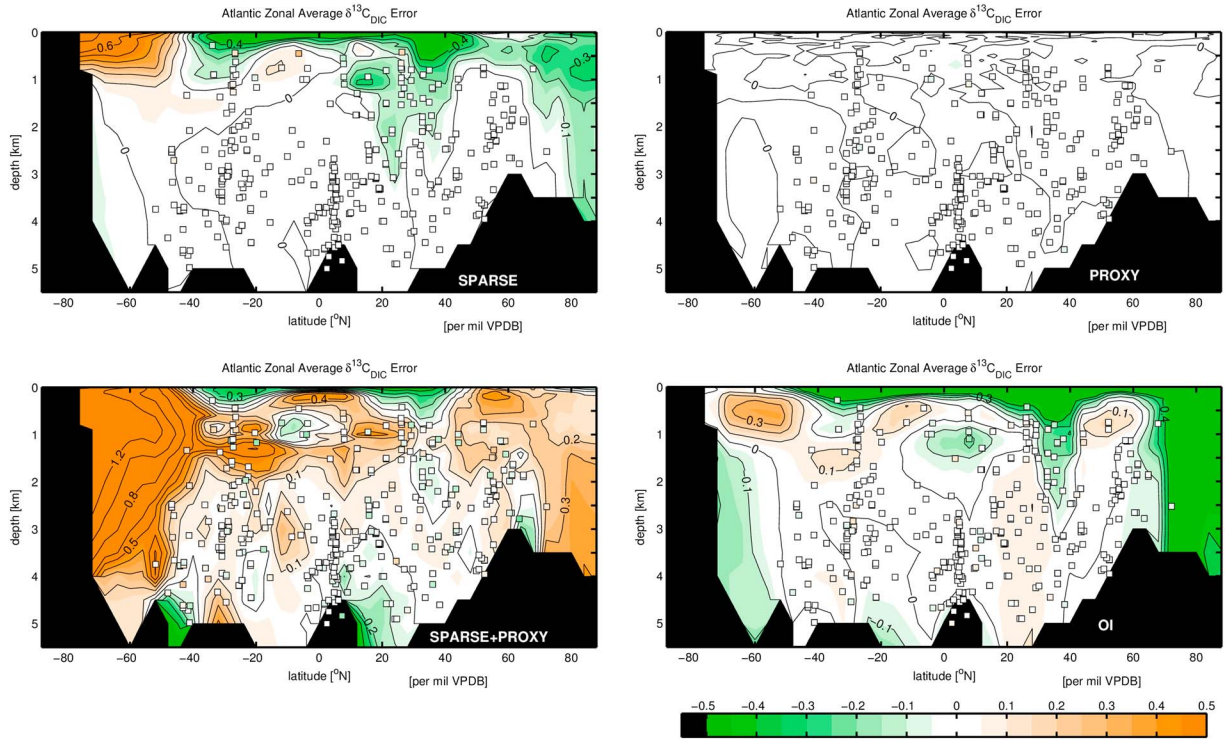

Figure 8. Basinwide zonal average Atlantic $\delta^{13}C_{DIC}$ errors (background contours) for the following cases: (top left) SPARSE, (top right) PROXY, (bottom left) SPARSE+PROXY, and (bottom right) OI. The pointwise misfit or error is reproduced for the subset of Atlantic observations (colored squares).

solution for better constraining the polar regions, but the surface would likely be improved by the addition of planktonic foraminiferal data.

3.3. Errors With Depth

In the following sections, we seek to quantify the reconstruction skill of the experiments. The vertical profile of the root-mean-square (RMS) error, $\sigma_o(z)$, is a skill metric that assesses whether the synthetic observations are adequately fit:

$$\sigma_o(z) = \left[\frac{1}{N_o(\hat{z})}\mathbf{n}_o(\hat{z})^T\mathbf{n}_o(\hat{z})\right]^{1/2}, \tag{2}$$

where "o" stands for observations, z is depth, $N_o(\hat{z})$ is the number of observations in a running depth interval ($\hat{z} = z \pm 250$ m), and $\mathbf{n}_o(\hat{z})$ is a vector composed of differences between the reconstructed and actual observations in that depth range. The error at the observational sites, $\sigma_o(z)$, is smaller than or similar to the $\delta^{13}C_{DIC}$ observational uncertainty of 0.15‰, a first check that the method is working correctly (Figure 9, left). If the random errors in the five trials are independent, the RMS error should decrease to roughly 0.07‰ ($\approx 0.15‰/\sqrt{5}$), and all experiments meet this standard as well (except for SPARSE in the data-void surface region where RMS errors are not well defined). Analysis with this basic metric confirms that the method skillfully reproduces the given observations, as expected, and also that no systematic errors as a function of depth are admitted.

To design a metric that diagnoses the skill at interpolation and extrapolation between observations, we introduce the vertical profile of RMS error at all grid cells:

$$\sigma_g(z) = \left[\frac{1}{N_g(\hat{z})}\mathbf{n}_g(\hat{z})^T\mathbf{n}_g(\hat{z})\right]^{1/2}, \tag{3}$$

where "g" stands for "grid," $N_g(\hat{z})$ is the number of grid cells in the 500 m running depth interval, and $\mathbf{n}_g(\hat{z})$ is a vector composed of a list of differences between the reconstructed and true fields in the depth interval. To put this metric in context, we define a zero skill level as the error incurred by using a climatological depth profile of $\delta^{13}C_{DIC}$ with no horizontal variability. In this case, the $\sigma_g(z)$ value is equal to the standard deviation of $\delta^{13}C_{DIC}$ values about the mean profile. For a conservative tracer in a steady state, this climatological variability must decrease as a function of depth, and $\delta^{13}C_{DIC}$ generally conforms to that expectation with the zero

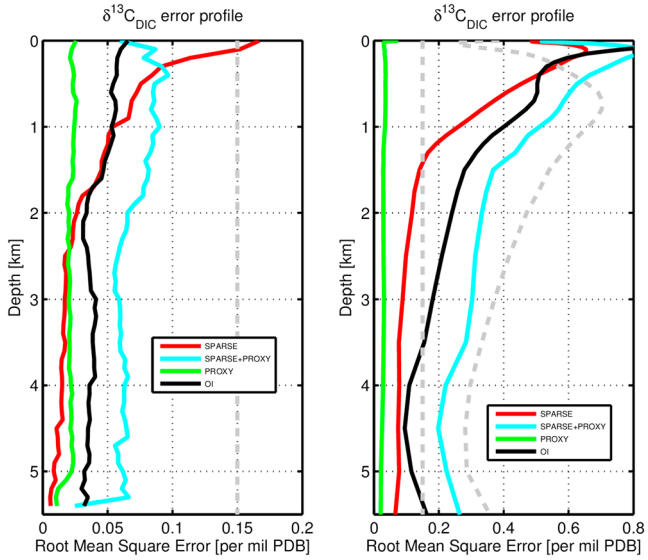

Figure 9. Vertical profile of the root-mean-square error of the reconstruction (left) at the observational sites, $\sigma_o(z)$ and (right) at every global grid point, $\sigma_g(z)$. The metrics are diagnosed for the SPARSE (red), SPARSE+PROXY experiments (cyan), PROXY (green), and OI (black) experiments. The 0.15‰ error level (vertical dashed gray line, both panels) is the noise level in the observations. For reference, the "zero skill" error level (rightmost dashed gray line, Figure 9, right) defined in the text is included for context.

skill level dropping from 0.7‰ at the surface to 0.3‰ at 5 km depth (rightmost dashed line, Figure 9, right). The local maximum at 750 m depth is due to horizontal variability by a sloping thermocline and the non-conservative effects resulting from the combination of the biological rain profile [e.g., *Martin et al.*, 1987] and increasing residence times with depth. Below 500 m depth, the three experiments that rely upon interpolation and extrapolation (SPARSE, SPARSE+PROXY, and OI) show skill relative to the zero skill level. Above 500 m depth, no observations have been used, thus explaining the lack of skill there.

When the skill metric, $\sigma_g(z)$, is less than 0.15‰ for $\delta^{13}C_{DIC}$ (leftmost dashed lines, Figure 9, right), the unobserved property values are being reproduced better than the original $\delta^{13}C_{DIC}$ uncertainty. When $\sigma_g(z)$ approaches 0.07‰, the withheld observations are being reproduced as well as would be expected if they were actually observed. The SPARSE reconstruction reproduces the withheld data everywhere below 1500 m, indicative of a surprising level of skill at interpolation and extrapolation over the majority of the ocean's volume (Figure 9, right). Despite the problem being mathematically underdetermined with many fewer observations than elements in the global $\delta^{13}C_{DIC}$ tracer distribution, the reconstruction method leverages the spatial correlations inherent in the kinematic model to make a skillful reconstruction. The OI experiment has a high skill level only below 3500 m depth, where the zero skill level and the observational uncertainty are not far apart. Thus, $\delta^{13}C_{DIC}$ has a signal-to-noise ratio of about 2 at these depths that limits its utility as a constraint. In contrast to the other cases, the SPARSE+PROXY experiment does not predict the withheld data at any depth level. That any of the experiments (e.g., SPARSE) could pass the stringent test posed by the $\sigma_g(z)$ metric is promising for the reconstruction of large-scale distributions from sparse paleoceanographic samples.

3.4. Errors With Distance From Observation

A recent LGM state estimate performed with a time-evolving general circulation model found that deep paleo-observations only served as a local constraint on seawater properties [*Dail and Wunsch*, 2014]. Here we wish to revisit the issue with the state estimation method that uses a true steady state model and thus does not require long time integrations. To do so, we modify the gridded error statistic, $\sigma_g(z)$, from the last subsection to be a function of horizontal distance, r_{xy}, and vertical distance, r_z, from a particular observation, i:

$$\sigma_g^i(r_{xy}, r_z) = \left[\frac{1}{N_g(\hat{r}_{xy}, \hat{r}_z)}\mathbf{n}_g(\hat{r}_{xy}, \hat{r}_z)^T\mathbf{n}_g(\hat{r}_{xy}, \hat{r}_z)\right]^{1/2}, \quad (4)$$

where the direction to the observation (i.e., east or west and up or down) is not taken into account. The gridded errors, $\mathbf{n}_g$, are binned according to distance class ($\hat{r}_{xy} = r_{xy} \pm 250$ km, $\hat{r}_z = r_z \pm 100$ m), and the RMS error

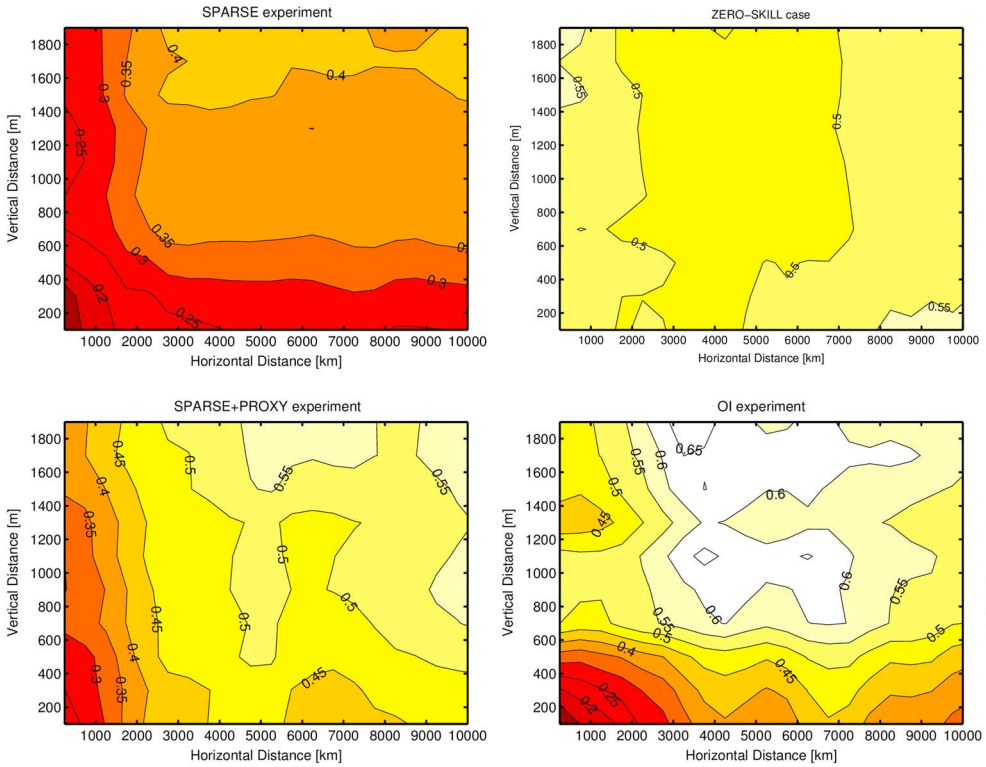

Figure 10. $\delta^{13}C_{DIC}$ RMS error, $\sigma_r(r_{xy}, r_z)$, as a function of horizontal distance (x axis) and vertical distance (y axis) from a given observation for the following experiments: (top left) SPARSE, (top right) zero skill, (bottom left) SPARSE+PROXY, and (bottom right) OI. Hotter colors represent the reconstruction being closer to the truth. The contour interval is 0.05‰ VPDB.

is computed with $N_g(\hat{r}_{xy}, \hat{r}_z)$ being the number of grid points in the class. Interpretation of equation (4) is complicated, because as one moves away from an observation, another one will be encountered. To make a statistic that (nearly) monotonically changes with distance, we compute $\sigma_g^i(r_{xy}, r_z)$ for each observation and then average across observations to make a single error function of distance,

$$\sigma_r(r_{xy}, r_z) = \frac{1}{N_{\text{obs}}} \sum_{i=1}^{N_{\text{obs}}} \sigma_g^i(r_{xy}, r_z), \tag{5}$$

where "r" stands for "range" and $N_{\text{obs}} = 492$ is the number of observations. The error distance function for the zero skill case (Figure 10, top right) has a uniform value of 0.5‰ consistent with the vertical average of the zero skill level (recall the rightmost dashed line in Figure 9, right). No observational information has been used in this estimate, and thus, the reconstruction has equal performance close or far from observations, which explains the nearly uniform distance function.

The error distance function, $\sigma_r(r_{xy}, r_z)$, has the smallest values near the origin ($r_{xy} = 0, r_z = 0$) for all cases, where the horizontal and vertical distances are short and observations provide the most information. The $\sigma_r(r_{xy}, r_z)$ values at the origin are similar to or less than 0.15‰ for the SPARSE, SPARSE+PROXY, and OI cases, consistent with the error estimates presented at the observational sites (recall Figure 9, left). The SPARSE case has the hottest colors (lowest values of $\sigma_r(r_{xy}, r_z)$) at all other distances indicating the greatest skill in extrapolation and interpolation. Errors are reduced relative to the zero skill case out to the largest spatial scales of 10,000 horizontal kilometers and 1500 vertical meters. The other experiments have less skill, specifically the SPARSE+PROXY case in the horizontal direction and the OI case in the vertical direction. As explained previously, the SPARSE+PROXY experiment has large horizontal gradients in the Atlantic sector of the Southern Ocean that result in increasing errors with increasing horizontal distance. The OI experiment relies upon prior statistical assumptions that effectively limit the spatial range over which interpolation and extrapolation can be accurately done; hence, the $\sigma_r(r_{xy}, r_z)$ error contours are concentrated near the origin. At points that are simultaneously more than 3000 horizontal kilometers and 800 vertical meters away from an observation, the

OI errors are greater than 0.6‰ and degraded relative to the zero skill baseline. Of course, our implementation of OI is crude, and we expect that improvement is possible given a more sophisticated handling of the input statistics (e.g., G. J. Streletz et al., submitted manuscript, 2016). Overall, the SPARSE case outperforms OI away from the observations with error values that are generally about 50% smaller, which we suggest is due to the use of a physical, rather than statistical, model. Thus, when observations are paired with this state estimation method, their influence is not limited to the local or regional area, but instead they constrain the largest oceanic scales.

4. Discussion

Visual and statistical measures indicate a gulf in the skill level between the SPARSE and SPARSE+PROXY experiments. One difference between the two experiments is how directly the state is observed. Another is the number of data types supplied at any observational location, where SPARSE has seven and SPARSE+PROXY has three. If conservative tracers are measured precisely with global coverage, only five such tracers are needed to determine the ocean pathways on a Cartesian grid, a consequence of the nature of steady state advection and diffusion of waters in three dimensions [*Gebbie and Huybers*, 2010]. During the LGM (and our analogous SPARSE+PROXY experiment), several hundred observations of benthic foraminiferal δ^{13}C, δ^{18}O, and Cd/Ca are available. Considering that $\delta^{13}C_{DIC}$ and Cd are both subject to nonconservative sources and can be combined to form the nearly conservative tracer $\delta^{13}C_{as}$ [e.g., *Lynch-Stieglitz et al.*, 1995], we have two independent conservative tracers in hand for the LGM, as opposed to the five tracers needed to disentangle the pathways of the large-scale ocean circulation. For this reason, we suggest that about three more paleo-observations are needed to make the SPARSE+PROXY results approach the accuracy of the SPARSE experiment. Candidates for the needed conservative tracers already exist. The isotope composition of the rare Earth element, Nd, is promising [*Roberts et al.*, 2010], as well as carbon-cycle tracers such a B/Ca that have been suggested to be close to conservative [e.g., *Yu and Elderfield*, 2007]. Temperature records (e.g., Mg/Ca and foraminiferal assemblages [*Skinner et al.*, 2003; *Kucera et al.*, 2006]) and radiocarbon [e.g., *Thornalley et al.*, 2015] are other possibilities. Challenges, such as measuring all these properties at the same locations and relating the proxies to seawater properties, would also have to be met.

A key issue in paleoceanography is the representativeness of any point observation for the large-scale circulation. To what extent do observations represent local, regional, or global processes? Here we find that the answer depends upon the reconstruction method. The SPARSE and OI experiments, for example, differ in the reconstruction method used and make a nice case study. The SPARSE experiment uses the state estimation method that includes circulation pathways as a logical basis for making a gridded field from sparse observations, and each δ^{13}C observation provides information both upstream and downstream under the steady state assumption. The pathway mapping technique explicitly builds circulation constraints into the map, and the resulting interpolation and extrapolation are more accurate than OI at long distances (recall Figure 10). Rather than characterizing the circulation statistically, as is done in OI, we use a simple kinematic tracer conservation model as a "dynamic interpolator" between far-flung data points. Additionally, the state estimates are superior in the sense that they permit circulation to be diagnosed, nonconservative effects to be inferred, and for tracer budgets to be calculated. Despite the additional constraints on state estimation, perhaps it is even surprising that large-scale property distributions are fit better than optimal interpolation in most metrics. Recent work has shown that circulation information can be supplied to an OI method, and we expect that this will help narrow the skill gap between the two methods (G. J. Streletz et al., submitted manuscript, 2016).

This work has focused on the paleoceanographically relevant $\delta^{13}C_{DIC}$ tracer, but a number of other quantities are inferred by the state estimation method. While the PROXY experiment is successful at reproducing the observations that were observed, does this experiment also accurately reconstruct the unobserved property distributions, such as the temperature, salinity, and mass fluxes? The gridded RMS error can be redefined from equation (3) to be one scalar for the entire globe: $\overline{\sigma_g} = \sqrt{\mathbf{n}_g^T \mathbf{n}_g / N_g}$, where N_g is the total number of grid points and $\mathbf{n}_g$ is a vector with the complete list of gridded errors. To put this metric in context, the expected RMS error for a least squares problem can be computed from a χ^2 distribution and is here labeled, $<\overline{\sigma_g}>$. The ratio, $\overline{\sigma_g}/<\overline{\sigma_g}>$, should be near 1 for a skillful reconstruction of the withheld data, but here we find that none of the other tracers are well produced (Θ : 10.1, S_* : 151.5,PO_4 : 2.7,NO_3 : 23.2,O_2 : 17.2). The values for this metric are proportional to the signal-to-noise ratio in each observational type, explaining the obtained range. The results are likely due to the indirect measurement of the state properties, like temperature,

by the paleoceanographic proxies. In addition, the model used for state estimation is purely kinematic and lacks a number of processes that relate temperature and salinity to the geometry of water masses through geostrophic balance. If the full information contained in paleoceanographic proxies is to be extracted, state estimation should use a dynamic, not just kinematic, model.

5. Conclusion

A distinguishing feature of paleoceanography is the difficulty in obtaining observations, and for those observations to be sparse proxies of the physical and biogeochemical properties of interest. To understand how the paleoceanographic data sampling may limit our view of the past ocean circulation, we devise an idealized experiment that samples the modern-day ocean with sparse, proxy observations to evaluate how well the global seawater property distributions can be reconstructed. We use 492 synthetic observations of $\delta^{13}C$, $\delta^{18}O$, and Cd/Ca at the core sites compiled by *Peterson et al.* [2014] to constrain a tracer transport model through a state estimation method. Under the perfect model assumption of this study, the Atlantic-Pacific $\delta^{13}C_{DIC}$ difference is recoverable, but the vertical structure of the circulation is unlike the known modern-day circulation and the spreading of North Atlantic Deep Water into the South Atlantic is obscured. Instead, a circulation that is symmetric about the equator in all ocean basins with a relatively strong biological pump is capable of fitting all of the synthetic paleodata. That the state estimation method reconstructs this scenario is dependent upon the assumed prior information, and here, the experiment is designed to assume the bare minimum in an attempt to not bias the result with any modern-day oceanographic information. The actual case of reconstructing the Last Glacial Maximum is undoubtedly somewhat easier because the modern-day circulation could be considered a reasonable first guess for glacial conditions; however, the perfect model assumption of this study does not apply.

Two further experiments are posed in which paleoceanographic-like observations are taken from the known modern-day circulation, but the sparsity and proxy nature of the observations are isolated. If the three proxy data types are taken everywhere on the global grid with a realistic error level, isolating the proxy nature of paleodata, the global property distributions can be accurately reconstructed. If a suite of modern-day tracers is sampled at the paleoceanographic data sites, isolating the sparsity of paleodata, again the global property distributions can be reconstructed with a state estimation method. In the latter case, the incursion of NADW into the South Atlantic is clearly seen, the abyssal pattern of aging from the Atlantic to Pacific Oceans is captured, and the withheld data below 1500 m depth are accurately predicted despite being unobserved. This succession of experiments shows that as the number of observed data types is increased from three to seven, the large-scale circulation comes into focus, even if observations are as sparse as recent LGM compilations. Thus, the sparsity of paleodata is not the limiting factor for our ability to reconstruct past ocean property distributions at the largest spatial scales, but instead, it is the number of independent constraints that we can place on the circulation.

The inferences of this work depend upon the reconstruction method used, as we find that state estimation with a tracer transport model is superior at interpolation and extrapolation over long distances relative to an optimal interpolation method. When paleoceanographic observations are used to constrain a state estimate, our error statistics indicate that useful information can be extracted out to the largest ocean scales: at least 10,000 km horizontally and 1500 m vertically. These statistics quantify the extent to which paleodata are representative of regional and global phenomena relative to local processes. Paleoceanographic work on additional tracers and their interpretation, including planktonic data that are ignored here, should yield fruitful results in future glacial state estimates.

Appendix A: Tracer Equations

The tracer equations are based upon the flux form of the advection-diffusion equation in steady state: $\nabla \cdot [\rho \vec{u} C - \rho \kappa \nabla C] = Q$, where ρ is the density, $\vec{u}$ is the 3-D velocity field, C is the tracer concentration, κ is the diffusion tensor, and Q is the nonconservative source in units of the tracer value per second. Discretizing with a centered-space scheme on a staggered C grid, the equation for a grid cell denoted "j" that has N neighbors is

$$\sum_{i=1}^{N} \{ c_i \left[\rho_{ij} A_{ij} \left(\frac{u_{ij}}{2} + \frac{\kappa_{ij}}{\Delta x_{ij}} \right) \right] - c_j \left[\rho_{ij} A_{ij} \left(\frac{u_{ij}}{2} + \frac{\kappa_{ij}}{\Delta x_{ij}} \right) \right] \} = -QM_j, \tag{A1}$$

where c_i is the tracer concentration in cell i, ρ_{ij} is the average of the densities in grid cells i and j, u_{ij} is the velocity from cells i to j, κ_{ij} is the diffusivity on the face shared by cells i and j with area, A_{ij}, Δx_{ij} is the distance between cell centers, and M_j is the mass of cell j. Equation (A1) can be rearranged to have the same form as the water mass equation (1) in the main text: $c_j = \sum_i^N m_{ij} c_i + q_j$. By inspection, we identify the following relationships,

$$m_{ij} = \frac{\rho_{ij} A_{ij} (\frac{u_{ij}}{2} + \frac{\kappa_{ij}}{\Delta x_{ij}})}{\sum_{k=1}^{N} \rho_{kj} A_{kj} (\frac{\kappa_{kj}}{\Delta x_{kj}})}, q_j = \frac{QM_j}{\sum_{k=1}^{N} \rho_{kj} A_{kj} (\frac{\kappa_{kj}}{\Delta x_{kj}})}, \tag{A2}$$

where m_{ij} represents the nondimensional mass-flux ratio and q_j is the nonconservative source in units of tracer concentration. The denominators in (A2) have been simplified by invoking the conservation of mass: $\sum_{i=1}^{N} \rho_{ij} A_{ij} u_{ij} = 0$, as found by substituting $c_i = c_j = 1$ into equation (A1).

Both advective and diffusive processes are implicit in the water mass formulation of the tracer equations, despite the fact that the expressions in (A2) are nondimensionalized by a grid cell-specific timescale and thus contain no direct rate information. Note that the combination of velocity and diffusivity values must be limited in some way to keep the tracer concentration nonnegative (i.e., $0 \leq m_{ij} \leq 1$), as is done in flux-limited advection-diffusion schemes. Such limits will depend upon the differencing scheme, as can be confirmed if upwind differencing is performed instead of centered-space differencing.

A1. First Guess for Mass Flux Ratios

We wish to impose as little information as possible into our first guess for the mass flux ratios, m_{ij}. For a conservative tracer ($Q = 0$), the steady state tracer equations can be satisfied with vanishing velocity and diffusivity fields, where the observed tracer distribution is a "standing stock." Taking equation (A2) in the limit that the velocity vanishes and the diffusivity tends to zero, m_{ij} is well defined by L'Hôpital's rule:

$$\lim_{\kappa \to 0} m_{ij} = \frac{\rho_{ij} A_{ij}}{\Delta x_{ij}} / (\sum_{k=1}^{N} \frac{\rho_{kj} A_{kj}}{\Delta x_{kj}}) \approx 1/N, \tag{A3}$$

where the approximation is strictly true if κ is uniform (as might be the case for molecular diffusivity), density is uniform, and the grid cell is a cube. The approximation also holds well with typical modern-day values of eddy diffusivity on our global grid and is used here for the first-guess mass flux ratios.

Appendix B: State Estimation Method

The search for three-dimensional property distributions that are consistent with observations and a numerical model is here referred to as state estimation [e.g., *Wunsch*, 1996]. The problem is formalized as the least squares problem of minimizing a sum of squared misfits between estimated and observed tracer distributions subject to prior information and a model (following the description in *Gebbie* [2014])

$$J = (\mathbf{Ex} - \mathbf{y})^T \mathbf{W}^{-1} (\mathbf{Ex} - \mathbf{y}) + \mathbf{u}^T \mathbf{S}^{-1} \mathbf{u} + \mu^T \mathcal{F}[\mathbf{x}, \mathbf{u}], \tag{B1}$$

where J is the function to be minimized, $\mathbf{x}$ is the state vector, $\mathbf{y}$ contains a suite of tracer observations, $\mathbf{E}$ is a matrix that maps the state vector onto the observations, ^{T} is the matrix transpose, $\mathbf{u}$ is the control vector of unknowns, $\mathbf{W}$ and $\mathbf{S}$ are weighting matrices, μ is a Lagrange multiplier vector, and $\mathcal{F}[\mathbf{x}, \mathbf{u}] = \sum_i^N m_{ij} c_i - c_j + q_j = 0$ is the constraint on mass and each state variable tracer type (i.e., a rearrangement of the "model" equations). The state vector includes the three-dimensional property fields, the circulation in terms of mass flux ratios, and any sources or sinks, i.e., $\mathbf{x} = [\mathbf{c}_k; \mathbf{m}; \mathbf{q}]^T$, for all state variables, k. The only alteration for the SPARSE, PROXY, and SPARSE+PROXY cases is the observational cost function term (first term on the right-hand side of (B1)).

The state vector includes the conservative tracers Conservative Temperature (Θ), preformed salinity (S_*), and $\delta^{18}O_w$, which are modeled with the source or sink being identically zero ($q_j = 0$ for all j). $\delta^{13}C_{DIC}$ is modeled as a nonconservative tracer due to biological effects, and its sink in the interior is modeled as being proportional to an increase in PO_4 with a ratio of $-1.1‰ : 1$ μmol/kg [e.g., *Broecker and Maier-Reimer*, 1992].

The state vector can be varied in directions imposed by the control equation: $\mathbf{x} = \mathbf{x}_0 + \Gamma \mathbf{u}$, where Γ maps the control vector onto the state. The Lagrange multiplier term (third term on the right-hand side of (B1)) enforces the steady state tracer equations. The constrained least squares problem is solved by hand-coding an adjoint model that renders the computations more tractable by modeling each seawater property in series, and using adjoint-computed sensitivity information to guide a variable-storage quasi-Newton optimization method [*Nocedal*, 1980].

B1. Updates to the Thermodynamic Equation of State

The state estimation method [*Gebbie*, 2014] is updated to incorporate the thermodynamic equation of state [*IOC et al.*, 2010] by transferring the state variables from potential temperature and practical salinity to Conservative Temperature and preformed salinity. For this thought experiment, we do not wish the atlas of seawater compositional changes from the modern ocean to be available, as we do not want a modern-day bias in the results. Instead, compositional changes in absolute salinity are related to phosphate via the relation: $\delta S_A = (4.12 \times 10^{-5}) \times \exp(2[PO_4])$, which fits the modern day with an error of 0.006 g/kg. This approximation is not quite as accurate as the modern-day regression between silicate and absolute salinity [*McDougall et al.*, 2012], but silicate is not available here as one of the state variables.

Appendix C: Optimal Interpolation Formulation

Our implementation of optimal interpolation assumes that the first- and second-order statistics of the $\delta^{13}C_{DIC}$ distribution are available:

$$< \mathbf{x} > = \bar{c}, < \mathbf{x}(\mathbf{r}_i, \mathbf{r}_j)\, \mathrm{x}(\mathbf{r}_i, \mathbf{r}_j)^T > = \mathbf{R}_{xx}(\mathbf{r}_i, \mathbf{r}_j), \tag{C1}$$

where the brackets indicate the expected value, the state vector, $\mathbf{x}$, only includes $\delta^{13}C_{DIC}$, a scalar baseline is defined (i.e., $\bar{c} = 0.7‰$ that corresponds to the mean of the true $\delta^{13}C_{DIC}$ vector), and $\mathbf{r}_i$ and $\mathbf{r}_j$ are 3-D vectors of positions. We seek an estimate, $\tilde{\mathbf{x}}$, whose dispersion about the true solution, $\mathbf{x}$,

$$\mathbf{P} = < (\tilde{\mathbf{x}} - \mathbf{x})(\tilde{\mathbf{x}} - \mathbf{x})^T >, \tag{C2}$$

is as small as possible. The covariance function is prescribed as a Gaussian function of the number of grid points away,

$$\mathbf{R}_{xx} = P_0 \exp[-(|\mathbf{r}_i - \mathbf{r}_j|/L_2)^2], \tag{C3}$$

where $P_0 = 1‰$ and $L_2 = 8$ grid points. We use a Gaussian covariance function where the covariance is set to be identically zero when 10 or more lengthscales away from the grid point, thus making $\mathbf{R}_{xx}$ a sparse matrix and improving computational efficiency. Observational statistics are also assumed available: $\mathbf{R}_{nn} = \sigma_n^2 \mathbf{I}$, where $\sigma_n = 0.15‰$ and $\mathbf{I}$ is the identity matrix. Then the optimal interpolation estimate is [*Wunsch*, 1996]

$$\tilde{\mathbf{x}} = \bar{c} + \mathbf{R}_{xx}\mathbf{E}^T(\mathbf{E}\mathbf{R}_{xx}\mathbf{E}^T + \mathbf{R}_{nn})^{-1}(\mathbf{y} - \bar{c}) \tag{C4}$$

and is calculated with sparse matrix multiplication and division algorithms.

Acknowledgments

The reference modern-day tracer distributions are available at https://www.whoi.edu/website/ggebbie/ under the downloads page. Supporting data including the specific locations and values of the synthetic observations are included as a CSV text file. Any additional data, including MATLAB codes, may be obtained from G.G. (ggebbie@whoi.edu). The authors thank Tom Chalk and Carl Wunsch for comments on the manuscript and Tor Eldevik, Steve Jayne, Peter Huybers, Louise Kellogg, Lorraine Lisiecki, Carlye Peterson, and Pelle Robbins for discussions. This work was supported by NSF grants 1124880 (G.G.) and 1125422 (H.J.S.).

References

Bemis, B., H. Spero, J. Bijma, and D. Lea (1998), Reevaluation of the oxygen isotopic composition of planktonic foraminifera: Experimental results and revised paleotemperature equations, *Paleoceanography*, *13*(2), 150–160.

Brady, E. C., B. L. Otto-Bliesner, J. E. Kay, and N. Rosenbloom (2013), Sensitivity to glacial forcing in the CCSM4, *J. Clim.*, *26*(6), 1901–1925.

Bretherton, F., R. Davis, and C. Fandry (1976), A technique for objective analysis and design of oceanographic experiments applied to MODE-73, *Deep Sea Res.*, *23*, 559–582.

Broecker, W., and E. Maier-Reimer (1992), The influence of air and sea exchange on the carbon isotope distribution in the sea, *Global Biogeochem. Cycles*, *6*(3), 315–320.

Broecker, W. S., and G. H. Denton (1989), The role of ocean-atmosphere reorganizations in glacial cycles, *Geochim. Cosmochim. Acta*, *53*, 2465–2501.

Broecker, W. S., and T. H. Peng (1982), *Tracers in the Sea*, Lamont-Doherty Earth Observatory of Columbia Univ., Palisades, New York.

Burke, A., O. Marchal, L. Bradtmiller, J. McManus, and R. François (2011), Application of an inverse method to interpret 231Pa/230Th observations from marine sediments, *Paleoceanography*, *26*, PA1212, doi:10.1029/2010PA002022.

Curry, W., and D. Oppo (2005), Glacial water mass geometry and the distribution of $\delta^{13}C$ of σCO_2 in the Western Atlantic Ocean, *Paleoceanography*, *20*, PA1017, doi:10.1029/2004PA001021.

Dail, H., and C. Wunsch (2014), Dynamical reconstruction of upper-ocean conditions in the Last Glacial Maximum Atlantic, *J. Clim.*, *27*(2), 807–823.

Divins, D. (2003), *Total Sediment Thickness of the World's Oceans and Marginal Seas*, NOAA Natl. Geophys. Data Cent., Boulder, Colo.

Duplessy, J., N. Shackleton, R. Matthews, W. Prell, W. Ruddiman, M. Caralp, and C. Hendy (1984), ^{13}C record of benthic foraminifera in the last interglacial ocean: Implications for the carbon cycle and the global deep water circulation, *Quat. Res.*, *21*(2), 225–243.

Elderfield, H., and R. Rickaby (2000), Oceanic Cd/P ratio and nutrient utilization in the glacial Southern Ocean, *Nature*, *405*(6784), 305–310.

Ganachaud, A. (2003), Error budget of inverse box models: The North Atlantic, *J. Atmos. Oceanic Tech.*, *20*(11), 1641–1655.

Gebbie, G. (2014), How much did Glacial North Atlantic Water shoal?, *Paleoceanography*, *29*(3), 190–209.

Gebbie, G., and P. Huybers (2006), Meridional circulation during the Last Glacial Maximum explored through a combination of $\delta^{18}O$ observations and a geostrophic inverse model, *Geochem. Geophys. Geosyst.*, *7*, Q11N07, doi:10.1029/2006GC001383.

Gebbie, G., and P. Huybers (2010), Total matrix intercomparison: A method for resolving the geometry of water-mass pathways, *J. Phys. Oceanogr.*, *40*(8), 1710–1728, doi:10.1175/2010JPO4272.1.

Gebbie, G., and P. Huybers (2012), The mean age of ocean waters inferred from radiocarbon observations: Sensitivity to surface sources and accounting for mixing histories, *J. Phys. Oceanogr.*, *42*(2), 291–305, doi:10.1175/JPO-D-11-043.1.
Gebbie, G., P. Heimbach, and C. Wunsch (2006), Strategies for nested and eddy-permitting state estimation, *J. Geophys. Res.*, *111*, C10073, doi:10.1029/2005JC003094.
Gebbie, G., C. D. Peterson, L. E. Lisiecki, and H. J. Spero (2015), Global-mean $\delta^{13}C$ and its uncertainty in a glacial state estimate, *Quat. Sci. Rev.*, *125*, 144–159, doi:10.1016/j.quascirev.2015.08.010.
Gherardi, J., L. Labeyrie, J. McManus, R. Francois, L. Skinner, and E. Cortijo (2005), Evidence from the Northeastern Atlantic basin for variability in the rate of the meridional overturning circulation through the last deglaciation, *Earth Planet. Sci. Lett.*, *240*(3–4), 710–723.
Gherardi, J., L. Labeyrie, S. Nave, R. Francois, J. McManus, and E. Cortijo (2009), Glacial-interglacial circulation changes inferred from 231Pa/230Th sedimentary record in the North Atlantic region, *Paleoceanography*, *24*, PA2204, doi:10.1029/2008PA001696.
Gouretski, V., and K. Koltermann (2004), WOCE global hydrographic climatology, *Tech. Rep. 35*, Berichte des Bundesamtes für Seeschifffahrt und Hydrographie.
Huybers, P., G. Gebbie, and O. Marchal (2007), Can paleoceanographic tracers constrain meridional circulation rates?, *J. Phys. Oceanogr.*, *37*(2), 394–407, doi:10.1175/JPO3018.1.
IOC, SCOR, and IAPSO (2010), The international thermodynamic equation of seawater—2010: Calculation and use of thermodynamic properties, 196 pp., Intergovernmental Oceanographic Commission, Manuals and Guides No. 56, UNESCO (English).
Keigwin, L., and E. Boyle (2008), Did North Atlantic overturning halt 17,000 years ago?, *Paleoceanography*, *23*, PA1101, doi:10.1029/2007PA001500.
Keigwin, L. D., and T. P. Guilderson (2009), Bioturbation artifacts in zero-age sediments, *Paleoceanography*, *24*, PA4212, doi:10.1029/2008PA001727.
Key, R. M., A. Kozyr, C. L. Sabine, K. Lee, R. Wanninkhof, J. L. Bullister, R. A. Feely, F. J. Millero, C. Mordy, and T.-H. Peng (2004), A global ocean carbon climatology: Results from Global Data Analysis Project (GLODAP), *Global Biogeochem. Cycles*, *18*, GB4031, doi:10.1029/2004GB002247.
Key, R. M., et al. (2010), The CARINA data synthesis project: Introduction and overview, *Earth Syst. Sci. Data*, *2*, 105–121.
Köhl, A., and J. Willebrand (2002), An adjoint method for the assimilation of statistical characteristics into eddy-resolving ocean models, *Tellus*, *54*(4), 406–425.
Kucera, M., A. Rosell-Mele, R. Schneider, C. Waelbroeck, and M. Weinelte (2006), Multiproxy approach for the reconstruction of the glacial ocean surface (MARGO), *Quat. Sci. Rev.*, *24*, 813–819.
Kurahashi-Nakamura, T., M. Losch, and A. Paul (2014), Can sparse proxy data constrain the strength of the Atlantic meridional overturning circulation?, *Geosci. Model Dev.*, *7*(1), 419–432.
Legrand, P., and C. Wunsch (1995), Constraints from paleotracer data on the North-Atlantic circulation during the last glacial maximum, *Paleoceanography*, *10*, 1011–1045.
Lisiecki, L., M. Raymo, and W. Curry (2008), Atlantic overturning responses to Late Pleistocene climate forcings, *Nature*, *456*(7218), 85–88.
Liu, Z., S.-I. Shin, R. S. Webb, W. Lewis, and B. L. Otto-Bliesner (2005), Atmospheric CO_2 forcing on glacial thermohaline circulation and climate, *Geophys. Res. Lett.*, *32*, L02706, doi:10.1029/2004GL021929.
Lynch-Stieglitz, J., T. Stocker, W. Broecker, and R. Fairbanks (1995), The influence of air-sea exchange on the isotopic composition of oceanic carbon: Observations and modeling, *Global Biogeochem. Cycles*, *9*(4), 653–665.
Marchal, O., and W. Curry (2008), On the abyssal circulation in the glacial Atlantic, *J. Phys. Oceanogr.*, *38*(9), 2014–2037.
Marchitto, T., and W. Broecker (2006), Deep water mass geometry in the glacial Atlantic Ocean: A review of constraints from the paleonutrient proxy Cd/Ca, *Geochem. Geophys. Geosyst.*, *7*, Q12003, doi:10.1029/2006GC001323.
Marchitto, T., W. Curry, J. Lynch-Stieglitz, S. Bryan, K. Cobb, and D. Lund (2014), Improved oxygen isotope temperature calibrations for cosmopolitan benthic foraminifera, *Geochim. Cosmochim. Acta*, *130*, 1–11.
Martin, J. H., G. A. Knauer, D. M. Karl, and W. W. Broenkow (1987), VERTEX: Carbon cycling in the northeast Pacific, *Deep Sea Res. A.*, *34*(2), 267–285.
McDougall, T., D. Jackett, F. Millero, R. Pawlowicz, and P. Barker (2012), A global algorithm for estimating absolute salinity, *Ocean Sci.*, *8*(6), 1123–1134.
McGillicuddy, D., D. Lynch, P. Wiebe, J. Runge, E. Durbin, W. Gentleman, and C. Davis (2001), Evaluating the synopticity of the US GLOBEC Georges Bank broad-scale sampling pattern with observational system simulation experiments, *Deep Sea Res. Part II*, *48*(1), 483–499.
McManus, J. F., R. Francois, J.-M. Gherardi, L. D. Keigwin, and S. Brown-Leger (2004), Collapse and rapid resumption of Atlantic meridional circulation linked to deglacial climate changes, *Nature*, *428*, 834–837.
Nocedal, J. (1980), Updating quasi-Newton matrices with limited storage, *Math. Comput.*, *35*(151), 773–782.
Peeters, F. J., G.-J. A. Brummer, and G. Ganssen (2002), The effect of upwelling on the distribution and stable isotope composition of Globigerina bulloides and Globigerinoides ruber (planktic foraminifera) in modern surface waters of the NW Arabian Sea, *Global Planet. Change*, *34*(3), 269–291.
Peterson, C. D., L. E. Lisiecki, and J. V. Stern (2014), Deglacial whole-ocean $\delta^{13}C$ change estimated from 480 benthic foraminiferal records, *Paleoceanography*, *29*, 549–563.
Piotrowski, A. M., S. L. Goldstein, R. H. Sidney, R. G. Fairbanks, and D. R. Zylberberg (2008), Oscillating glacial northern and southern deep water formation from combined neodymium and carbon isotopes, *Earth Planet. Sci. Lett.*, *272*(1), 394–405.
Roberts, N., A. Piotrowski, J. McManus, and L. Keigwin (2010), Synchronous deglacial overturning and water mass source changes, *Science*, *327*(5961), 75–78.
Schmidt, G. A. (1999), Error analysis of paleosalinity calculations, *Paleoceanography*, *14*(3), 422–29.
Schmidt, G. A., G. R. Bigg, and E . J. Rohling (1999), Global Seawater Oxygen-18 Database - v1.21. [Available at http://data.giss.nasa.gov/o18data/.]
Schmittner, A., N. Gruber, A. C. Mix, R. M. Key, A. Tagliabue, and T. K. Westberry (2013), Biology and air-sea gas exchange controls on the distribution of carbon isotope ratios ($\delta^{13}C$) in the ocean, *Biogeosci. Discuss.*, *10*(5), 8415–8466, doi:10.5194/bgd-10-8415-2013.
Skinner, L. C., N. J. Shackleton, and H. Elderfield (2003), *Millennial-Scale Variability of Deep-Water Temperature and $\delta^{18}O_{dw}$ Indicating Deep-Water Source Variations in the Northeast Atlantic, 0–34 cal. ka BP*, vol. 4, 1098.
Spero, H. J., J. Bijma, D. W. Lea, and B. E. Bemis (1997), Effect of seawater carbonate concentration on foraminiferal carbon and oxygen isotopes, *Nature*, *390*(6659), 497–500.
Stammer, D. (1997), Global characteristics of ocean variability estimated from regional TOPEX/Poseidon altimeter measurements, *J. Phys. Oceanogr.*, *27*, 1743–1769.
Stouffer, R., et al. (2006), Investigating the causes of the response of the thermohaline circulation to past and future climate changes, *J. Clim.*, *19*(8), 1365–1387.

Thornalley, D., H. Bauch, G. Gebbie, W. Guo, M. Ziegler, S. Bernasconi, S. Barker, L. Skinner, and J. Yu (2015), A warm and poorly ventilated deep Arctic Mediterranean during the last glacial period, *Science*, *349*(6249), 706–710.

Troupin, C., et al. (2012), Generation of analysis and consistent error fields using the data interpolating variational analysis (DIVA), *Ocean Modell.*, *52–53*, 90–101, doi:10.1016/j.ocemod.2012.05.002.

Waelbroeck, C., L. Skinner, L. Labeyrie, J.-C. Duplessy, E. Michel, N. V. Riveiros, J.-M. Gherardi, and F. Dewilde (2011), The timing of deglacial circulation changes in the Atlantic, *Paleoceanography*, *26*, PA3213, doi:10.1029/2010PA002007.

Wahba, G., and J. Wendelberger (1980), Some new mathematical methods for variational objective analysis using splines and cross validation, *Mon. Weather Rev.*, *108*(8), 1122–1143.

Weber, S., S. S. Drijfhout, A. Abe-Ouchi, M. Crucifix, M. Eby, A. Ganopolski, S. Murakami, B. Otto-Bliesner, and W. R. Peltier (2007), The modern and glacial overturning circulation in the Atlantic ocean in PMIP coupled model simulations, *Clim. Past*, *3*(1), 51–64.

Winguth, A., D. Archer, E. Maier-Reimer, and U. Mikolajewicz (2000), Paleonutrient data analysis of the glacial Atlantic using an adjoint ocean general circulation model, in *Inverse Methods in Global Biogeochemical Cycles, Geophys. Monogr. Ser.*, edited by P. Kasibhatla et al., pp. 171–183, AGU, Washington, D. C.

Wunsch, C. (1996), *The Ocean Circulation Inverse Problem*, Cambridge Univ. Press, 437 pp., New York.

Yu, J., and H. Elderfield (2007), Benthic foraminiferal B/Ca ratios reflect deep water carbonate saturation state, *Earth Planet. Sci. Lett.*, *258*(1), 73–86.